CANCER

Structural analysis of BRCA1 reveals modification hotspot

Yanping Liang,[1]* William J. Dearnaley,[1]* A. Cameron Varano,[1,2] Carly E. Winton,[1,3] Brian L. Gilmore,[1] Nick A. Alden,[1] Zhi Sheng,[1,4] Deborah F. Kelly[1,3,4,5]†

Cancer cells afflicted with mutations in the breast cancer susceptibility protein (BRCA1) often suffer from increased DNA damage and genomic instability. The precise manner in which physical changes to BRCA1 influence its role in DNA maintenance remains unclear. We used single-particle electron microscopy to study the three-dimensional properties of BRCA1 naturally produced in breast cancer cells. Structural studies revealed new information for full-length BRCA1, engaging its nuclear binding partner, the BRCA1-associated RING domain protein (BARD1). Equally important, we identified a region in mutated BRCA1 that was highly susceptible to ubiquitination. We refer to this site as a modification "hotspot." Ubiquitin adducts in the hotspot region proved to be biochemically reversible. Collectively, we show how key changes to BRCA1 affect its structure-function relationship, and present new insights to potentially modulate mutated BRCA1 in human cancer cells.

INTRODUCTION

The breast cancer susceptibility protein (BRCA1) coordinates DNA repair through a variety of mechanisms designed to protect genetic material (*1*–*5*). BRCA1 performs these duties in association with its binding partner, the BRCA1-associated RING domain protein (BARD1). In the nucleus, the BRCA1-BARD1 heterodimer interacts with other repair proteins at DNA lesions to function as an E3 ubiquitin ligase (*6*–*8*). Through a series of exquisitely controlled steps, BRCA1-BARD1 facilitates the transfer of ubiquitin moieties to a variety of nuclear protein substrates (*9*). These ubiquitin adducts direct their bound substrates toward different fates, one of which involves correcting DNA damage.

Base excision repair (BER) is a process that corrects non–helix-distorting damage to DNA caused by conditions such as oxidation. BRCA1 plays an essential role in helping cells deal with oxidative conditions by triggering BER pathways through ubiquitin signaling (*10*, *11*). Cells harboring inherited mutations in the *BRCA1* gene cannot adequately deal with increased levels of reactive oxygen species (ROS) arising from estrogen metabolism. These inadequacies lead to functional deficiencies in BER, an accumulation of DNA insults, and widespread genomic instability—a known hallmark of cancer induction (*12*–*15*). Ultimately, the weakened state of mutated BRCA1 in oxidative environments supports disease progression.

We recently reported that a prevalent clinical mutation, *BRCA1*^{5382insC}, influences the manner in which BRCA1 itself is modified in cancer cells (*16*). The main type of modification identified on BRCA1^{5382insC} was K48-linked ubiquitin chains. In the nuclei of cancer cells, higher levels of ubiquitination correlated with lower levels of active BRCA1^{5382insC} and changes in its biochemical properties. These results complemented the work of other colleagues who identified ubiquitin attachment site on BRCA1 in ovarian cancer cells. This site, termed the "degron sequence," is proximal to the BRCA1 N-terminal RING domain (*17*). Although many studies have connected modifications in BRCA1 to changes in cellular activity, what remains missing from these analyses is the face of BRCA1.

Increasing our knowledge of BRCA1's three-dimensional (3D) structure can provide new insights into rational drug design and precision medicine. Structural information is currently available for the BRCA1-BARD1 RING domains (*18*) and the BRCA1 C-terminal (BRCT) region (*19*). However, the molecular architecture of full-length BRCA1 has not been determined. Current outstanding questions in the field that structural studies can address include the following: (i) How do clinical mutations in BRCA1 affect its structure-function relationship? (ii) Can mutated forms of BRCA1 be rescued or restored to normal? Similarly, the manner in which BRCA1 adapts to environmental changes or stressful conditions is poorly understood at the molecular level.

To begin tackling these issues, we used a combination of biochemical and structural biology tools. Specifically, we used single-particle electron microscopy (EM) to investigate differences among BRCA1-BARD1 structures derived from human breast cancer cells. We found a high degree of similarity between wild-type and mutated assemblies under normal growth conditions. During chemically induced oxidative stress, we found that a lysine-rich "hotspot" region on mutated BRCA1^{5382insC} was readily ubiquitinated. Structural evidence suggests that this hotspot encompasses the documented degron sequence of BRCA1. Excessive ubiquitination in this area of the protein may be related to the previously noted decreases in BRCA1^{5382insC} activity (*16*, *17*). Significantly, the enzymatic removal of ubiquitin moieties in the hotspot region restored the overall structure of mutated BRCA1 assemblies. Together, our work provides a new lens to view BRCA1 along with the opportunity to transform its molecular properties.

RESULTS

Wild-type BRCA1-BARD1 forms a stable clamp-like motif

To determine the 3D architecture of BRCA1-BARD1 natively formed in breast cancer cells (Fig. 1A), we used biochemical tools and single-particle EM imaging technology. Here, we focused on visualizing differences between wild-type and genetically mutated or modified BRCA1. Wild-type BRCA1-BARD1 heterodimers (~300 kDa) produced in the nucleus of primary ductal carcinoma cells [HCC70 line (*20*); American

[1]Virginia Tech Carilion Research Institute, Virginia Tech, Roanoke, VA 24016, USA. [2]Translational Biology, Medicine, and Health Graduate Program, Virginia Tech, Blacksburg, VA 24061, USA. [3]School of Biomedical Engineering and Science, Virginia Tech, Blacksburg, VA 24061, USA. [4]Virginia Tech Carilion School of Medicine, Virginia Tech, Roanoke, VA 24016, USA. [5]Department of Biological Sciences, Virginia Tech, Blacksburg, VA 24061, USA.
*These authors contributed equally to this work.
†Corresponding author. Email: debkelly@vt.edu

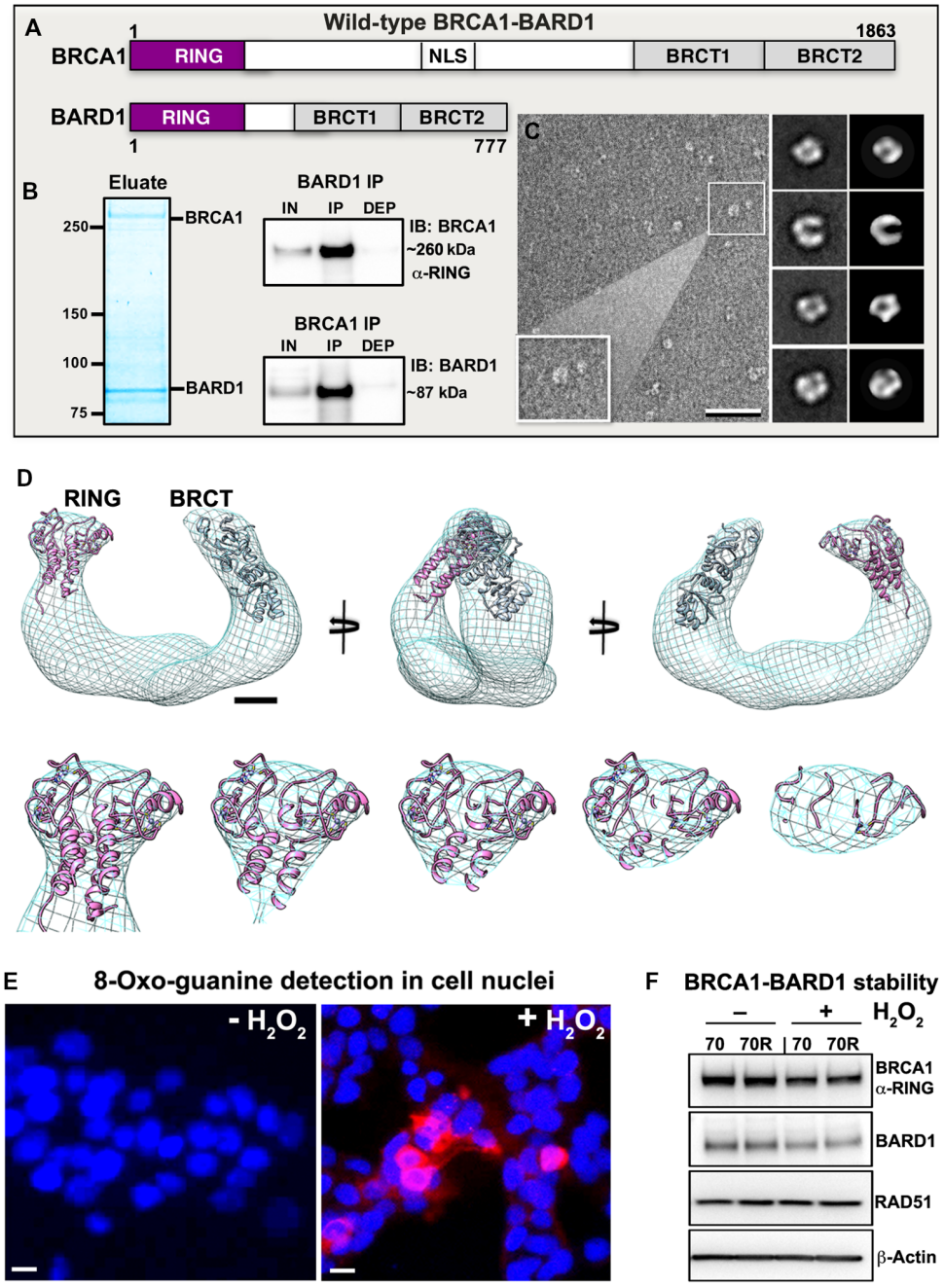

Fig. 1. The wild-type BRCA1-BARD1 EM structure resembles a clamp-like motif. (**A**) BRCA1 and BARD1 protein sequences show the N-terminal RING domains and C-terminal BRCT motifs. BRCA1 also contains central nuclear localization sequences (NLS). (**B**) Phosphorylated BRCA1 migrates at ~260 kDa, whereas BARD1 migrates at ~87 kDa according to SDS-PAGE. Western blots of the co-IP experiments identified interactions between BRCA1 and BARD1. (**C**) Image with inset of wild-type BRCA1-BARD1 (left) and corresponding 2D class averages (center). Scale bar, 50 nm. Projections of the 3D structure (right) agree with class averages. Box size, 25 nm. (**D**) The BRCA1-BARD1 EM map shows a clamp-like motif (movie S1). Atomic models for the BRCA1-BARD1 RING domain [magenta; PDB code, 1JM7 (*18*)] and the BRCT domain of BRCA1 [gray; PDB code, 1JNX (*19*)] were fit with the EM density based on antibody-labeling procedures (fig. S1 and movie S1). Scale bar, 1.5 nm. Cross sections through the RING domain show the quality of the model fit. (**E**) 8-OxoG formation (red) in the nuclei (blue) of HCC70 cells after treating with 1 mM H_2O_2 for 40 min. Untreated cells (– H_2O_2) did not accumulate 8-OxoG. Scale bars, 50 μm. (**F**) Western blots indicated relatively stable levels of BRCA1, BARD1, and RAD51 in HCC70 cells (70) and in cells resistant to oxidative stress (70R) during H_2O_2 treatment. Nuclear β-actin served as a loading control. IB, immunoblot; IN, input material; DEP, unbound/depleted material; IP, interacting proteins.

Type Culture Collection (ATCC)] were enriched by incubating nuclear extracts with nickel–nitrilotriacetic acid (Ni-NTA)–coated agarose beads. Phosphorylated BRCA1-BARD1 heterodimers involved in DNA damage response naturally bound to the beads and eluted in early fractions. The phosphorylated form of BRCA1 migrated at ~260 kDa on SDS–polyacrylamide gel electrophoresis (PAGE) analysis and BARD1 migrated at ~87 kDa (Fig. 1B).

To verify interactions between BRCA1 and BARD1, we performed coimmunoprecipitation (co-IP) experiments. Antibodies against BARD1 [Santa Cruz Biotechnology (SCBT)] or BRCA1 (C-20; SCBT)

were decorated onto protein G–labeled magnetic beads, and the protein fractions were incubated with the beads. The magnetically separated material was analyzed using Western blot detection. We identified BRCA1-BARD1 interactions by probing the blots with antibodies against the BRCA1 RING domain or against BARD1 (Fig. 1B). After confirming protein associations, we examined the BRCA1-BARD1 complexes using single-particle EM.

Low-dose images (<5 electrons/Å^2) were acquired for BRCA1-BARD1 specimens using an FEI Spirit BioTWIN transmission electron microscope (TEM) operating at 120 kV (Fig. 1C). Individual complexes were selected from the images using the SPIDER (System for Processing Image Data from Electron microscopy and Related fields) software package (*21*). Selected particles were subjected to standard reference-free alignment techniques also implemented in SPIDER. Class averages for wild-type BRCA1-BARD1 showed clamp-like structures with a diameter of ~120 Å (Fig. 1C). The particle images were imported into the RELION (REgularised LIkelihood OptimisatioN) software package (*22*) that was used to reconstruct and refine an EM density map (see Materials and Methods and table S1).

The 3D structure of wild-type BRCA1-BARD1 confirmed a clamp-like motif that was ~120 Å across its long axis and consistent with the class averages (Fig. 1D and movie S1). 2D projections of the 3D structure agreed with the class averages (Fig. 1C). Examining the density map in various orientations provides a conformational snapshot of the heterodimer in solution. The general molecular architecture of the complex resembled another recently determined E3 ubiquitin ligase structure of comparable molecular mass to BRCA1 (*23*).

To distinguish the BRCA1 RING domain from the BRCT region, we used EM affinity grids (*24*, *25*). Affinity grids were separately decorated with antibodies against each component (fig. S1). Atomic models of the RING [Protein Data Bank (PDB) code, 1JM7 (*18*)] and the BRCT [PDB code, 1JNX (*19*)] domains were placed in the density map according to positions defined by antibody-labeling results. The respective models could only fit in the density maps as indicated due to their unique features (Fig. 1D). The quality of the model fit is demonstrated in cross-sectional views shown in movie S1. The particles did not show limited orientations in their angular distribution, and the structure was refined to 14.5 Å according to the 0.5 Fourier shell correlation (FSC) criteria in RELION (fig. S1). The resolution of the map was verified using the RMEASURE application (*26*). The calculated molecular volume of the density map accommodates one BRCA1-BARD1 dimer.

Because expression levels and cellular stress can affect the functional response of BRCA1-BARD1 to DNA lesions, we tested for protein stability in breast cancer cells under stressful conditions. We induced oxidative stress by incubating cells with culture medium containing 1 mM hydrogen peroxide (H_2O_2) for up to 60 min, as previously described (*16*). Fluorescence microscopy was used to detect antibodies against 8-oxo-guanine (8-OxoG; SCBT) accumulation in genomic DNA. The formation of 8-OxoG is a direct marker for oxidative DNA damage in the nucleus.

After a 40-min incubation with H_2O_2, 8-OxoG signal (red fluorescence) increased in and around the nucleus of treated cells (blue fluorescence) (Fig. 1E). Control cells received culture medium lacking H_2O_2 and showed no signal for 8-OxoG during the incubation period. After 60 min of treatment, viability issues in treated cells limited measurements. As an additional control, HCC70 cells that experienced mild thermal stress before H_2O_2 treatment were also included in our analysis. These cells (HCC70-R) were primed to deal with cellular stress conditions and provided a model for oxidative resistance (*16*). Western blot comparisons of protein levels in treated cells showed that BRCA1 and BARD1 modestly decreased (~10 to 20%) in replicate experiments. As an independent control, we also assessed nuclear RAD51 levels and found little to no change in protein quantities during treatment. Nuclear β-actin served as a loading control for Western blot analyses. Overall, these results suggested that wild-type BRCA1 and BARD1 levels were relatively stable in the nucleus during oxidative conditions and DNA damage response.

How does the *BRCA1^{5382insC}* clinical mutation affect protein structure?

After gaining insight into wild-type BRCA1-BARD1, we focused on learning more about the *BRCA1^{5382insC}* cancer-related mutation. We hypothesized that the mutated BRCA1^{5382insC} protein may adopt a slightly different architecture. A frameshift mutation in the BRCA1^{5382insC} C terminus occurs at residue S1755, resulting in a ~10-kDa truncation (Fig. 2A). We performed the same biochemical procedures to isolate BRCA1^{5382insC}-BARD1 complexes from HCC1937 cells (ATCC) (*27*) that naturally express the mutated protein. According to SDS-PAGE analysis, BRCA1^{5382insC} migrated at ~260 kDa, similar to wild-type BRCA1. Subtle differences in protein conformation may account for the higher-than-expected mobility of mutated BRCA1. BARD1 migrated at ~87 kDa, and co-IP experiments confirmed BRCA1^{5382insC}-BARD1 interactions (Fig. 2B).

To determine the 3D structure of mutated BRCA1^{5382insC}-BARD1, we used the same imaging and computing procedures described for the wild-type assemblies. Individual particles were selected from images, and class averages were calculated using the SPIDER software package. The EM structure of the mutated BRCA1^{5382insC}-BARD1 complex revealed the same clamp-like motif seen in the wild-type structure (Fig. 2, C and D). The dimeric RING domain fits well within the N-terminal density, and a homology model of the mutated BRCT domain (*25*) was placed in the C-terminal region of the map. The BRCT density was somewhat reduced in the mutated structure, which is expected considering the truncation (Fig. 2D). Cross sections through the RING domain and EM density indicate the quality of the model fit from multiple views (movie S2). The particles did not show limited orientations in their angular distribution, and the structure was refined to 14.7 Å according to the 0.5 FSC criteria in RELION (fig. S2). The resolution was verified using the RMEASURE application.

A "modification hotspot" is identified on mutated BRCA1

Our recent biochemical studies showed that mutated BRCA1 was highly susceptible to ubiquitination under oxidative stress conditions (*16*). Comparatively, wild-type BRCA1 was not as susceptible to this effect. To understand the structural consequences of oxidative stress on mutated BRCA1, we performed EM analysis on protein assemblies isolated from HCC1937 cells treated with H_2O_2 (Fig. 3A). Images and class averages showed a clamp-like conformation, and particle dimensions were generally conserved in the treated BRCA1^{5382insC}-BARD1 complexes. One difference noted in the treated assemblies was a more compact shape than the untreated structures (Fig. 3A).

Taking a closer look at the protein components isolated from H_2O_2-treated cells, we found differences in SDS-PAGE and Western blot analysis. Mutated BRCA1^{5382insC} migrated at ~270 kDa after H_2O_2 treatment, whereas BARD1 primarily migrated at ~87 kDa (Fig. 3B). Another form of BARD1 was detected (~120 kDa), but it did not associate with BRCA1. We further examined the nuclear material of treated cells expressing BRCA1^{5382insC} or wild-type BRCA1 from two different

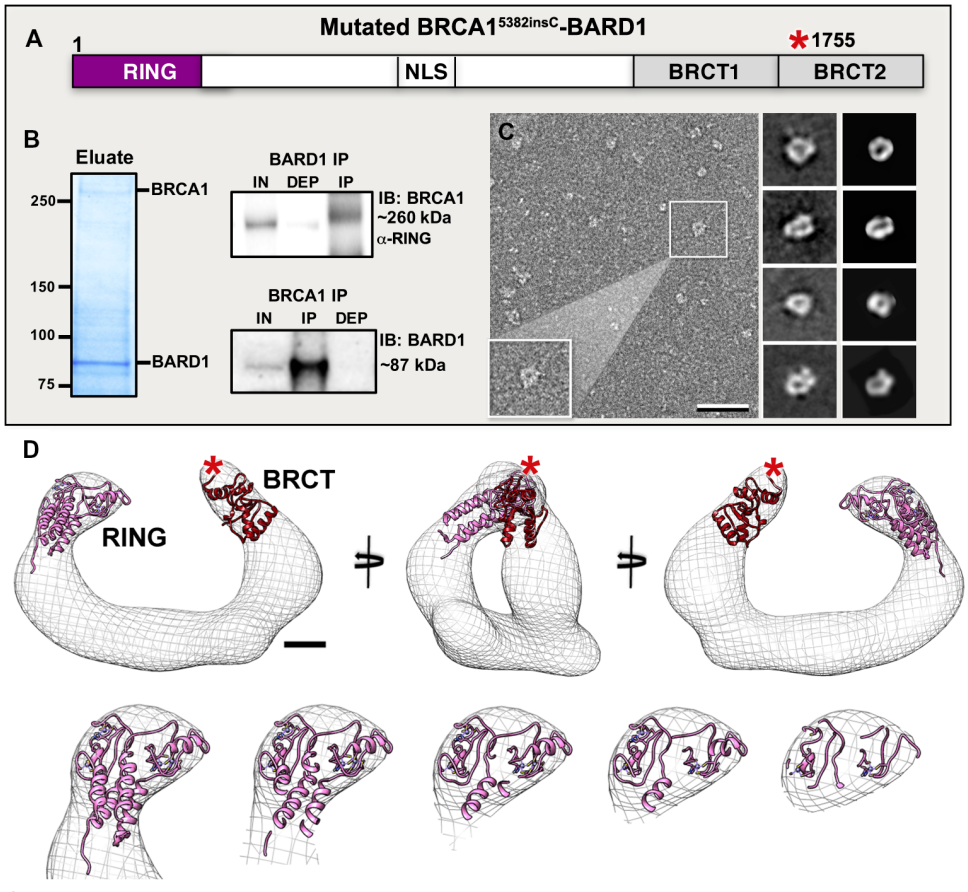

Fig. 2. The BRCA1^{5382insC}-BARD1 structure shows subtle variations from the wild-type structure. (**A**) The protein sequence of BRCA1^{5382insC} has a frameshift mutation at residue S1755 (red star). (**B**) BRCA1^{5382insC} migrates at ~260 kDa, and BARD1 migrates at ~87 kDa according to SDS-PAGE. Western blots of co-IP experiments identified interactions between mutated BRCA1 and BARD1. (**C**) Image with inset of BRCA1^{5382insC}-BARD1 (left) and corresponding 2D class averages (center). Scale bar, 50 nm. Projections of the 3D structure (right) agree with the class averages. Box size, 25 nm. (**D**) The 3D structure of BRCA1^{5382insC}-BARD1 reveals a clamp-like motif with defined RING and BRCT regions (movie S2). Scale bar, 1.5 nm. Molecular models for the RING domain of BRCA1-BARD1 [magenta; PDB code, 1JM7 (*18*)] and a homology model of the BRCT domain (*25*) fit in the envelope. The red star indicates the mutation site. Scale bar, 1.5 nm. Cross sections through the RING domain region show the model fit (fig. S2 and movie S2). IB, immunoblot; IN, input material; DEP, unbound/depleted material; IP, immunoprecipitated proteins.

sources (HCC70 and HCC70-R cells). Western blots revealed a major decline in the detection of BRCA1^{5382insC} using antibodies against the RING domain (Fig. 3C). This result may be due to decreased protein levels or limited accessibility near the BRCA1^{5382insC} RING epitope.

We calculated an EM density map for the BRCA1^{5382insC}-BARD1 complex isolated from H_2O_2-treated cells. The same imaging and computing methods were implemented in the SPIDER and RELION software packages. Models for the dimeric RING domain and mutated BRCT region fit well within the density as illustrated in Fig. 3D, fig. S3, and movie S3. Similar to the structures of wild-type and untreated complexes, particle orientations were not limited, and the map was refined to 15.6 Å according to the 0.5 FSC criteria determined in RELION and RMEASURE (fig. S3). The BRCA1^{5382insC}-BARD1 structure produced under oxidative stress conditions was more compact and had extra density adjacent to the RING domain (Fig. 3D).

To better understand these physical changes, we calculated a difference map between the H_2O_2-treated BRCA1^{5382insC}-BARD1 structure and the untreated BRCA1^{5382insC}-BARD1 structure. Difference densities at or above a 3σ threshold are considered statistically significant (*28*). On the basis of these criteria, conformational changes in the central portion of the structure and the BRCT regions were smaller in comparison to differences near the RING domain but were visibly present. We found a significant difference in the region proximal to the RING domain, which we refer to as a modification hotspot (Fig. 3D, fig. S3, and movie S3). The volume of the difference peak in the hotspot area (Fig. 3D, yellow) can accommodate a protein density of ~12 kDa, which is sufficient to contain at least one ubiquitin moiety. Previous studies identified this region on BRCA1 to contain a degron sequence (*17*). This degron site is a known target for K48 ubiquitination that can lead to proteasomal degradation of the protein. Therefore, we tested for BRCA1 stability in the nucleus of H_2O_2-treated cells.

Cells were incubated with 1 mM H_2O_2 for up to 40 min, and fluorescence microscopy was used to detect 8-OxoG formation in and around the nucleus of the cells. Untreated control cells expressing BRCA1^{5382insC} contained 8-OxoG foci, a signature of oxidative DNA damage, at the start of the experiment (Fig. 3E, red foci). The 8-OxoG signal in the untreated cells persisted throughout the experiments but did not increase. Treated cells accumulated greater levels of 8-OxoG during the 40-min incubation. These results suggested that cells expressing mutated BRCA1^{5382insC} were not well equipped to deal with

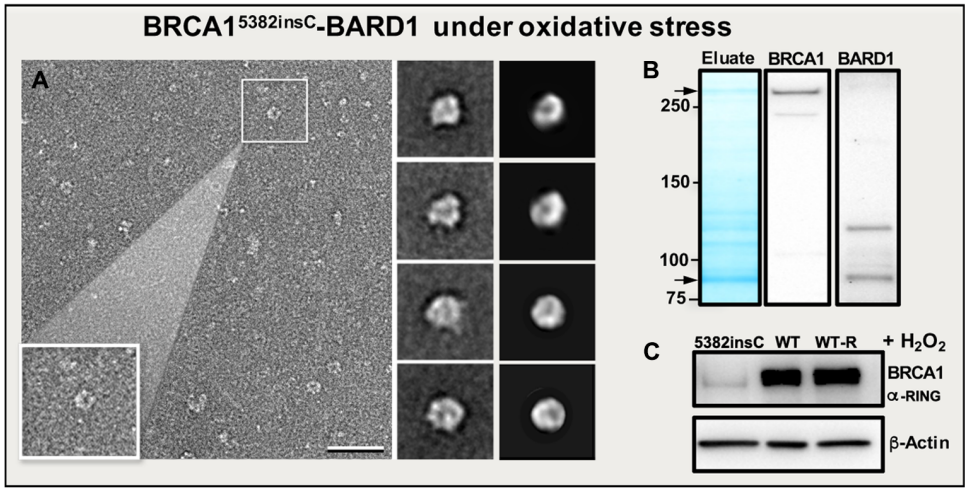

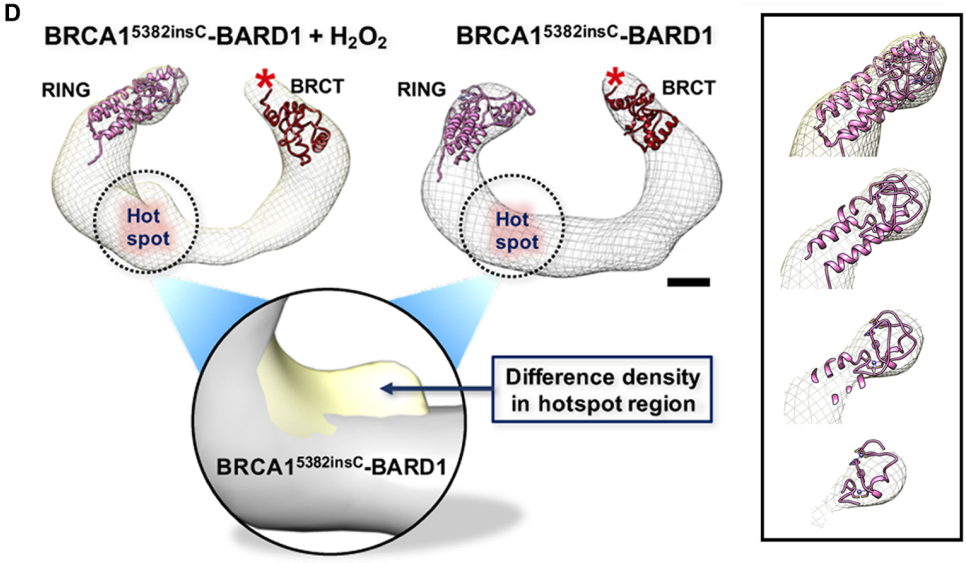

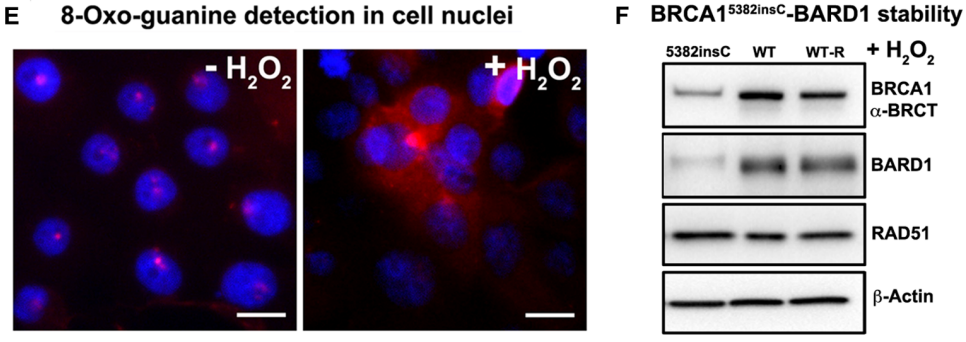

Fig. 3. Changes in the BRCA1^{5382insC}-BARD1 EM structure under oxidative pressure. (**A**) Image (left) and class averages (center) of mutated BRCA1^{5382insC}-BARD1 isolated from HCC1937 cells treated with 1 mM H_2O_2. Scale bar, 50 nm. Projections of the 3D structure (right) agree with the class averages. Box size of averages, 25 nm. (**B**) Under oxidative conditions, BRCA1^{5382insC} migrates at ~270 kDa, and BARD1 migrates at ~87 kDa according to SDS-PAGE and Western blot analysis. (**C**) After H_2O_2 treatment, the RING domain of BRCA1^{5382insC} was difficult to detect compared to wild-type BRCA1 (WT). Wild-type BRCA1 (WT-R) from treated HCC70-R cells is resistant to oxidative damage. Nuclear β-actin served as a loading control. (**D**) The BRCA1^{5382insC}-BARD1 structure shows a clamp-like motif with extra density adjacent to the RING domain (black circle). Scale bar, 1.5 nm. Atomic models for the RING domain [magenta; PDB code, 1JM7 (*18*)] and a homology model of the BRCT domain (*25*) fit in the molecular envelope (fig. S3 and movie S3). Difference peak (yellow) indicates the additional mass present in the hotspot region of BRCA1^{5382insC} under oxidative conditions. This additional mass was not present in the untreated BRCA1^{5382insC}-BARD1 density map (gray). The red star indicates the mutation site. Scale bar, 1.5 nm. Cross sections through the RING domain are indicated (movie S3). (**E**) 8-OxoG formation (red) in the nuclei (blue) of HCC1937 cells treated for 40 min with 1 mM H_2O_2. Untreated cells (– H_2O_2) had inherent 8-OxoG foci. Scale bar, 50 μm. (**F**) Western blots indicated unstable BRCA1^{5382insC} and BARD1 compared to RAD51 in treated HCC1937 cells. Nuclear β-actin served as a loading control.

oxidative conditions. This finding is important because ROS are produced during estrogen metabolism, giving rise to oxidated DNA lesions (*10*, *11*). Because cells expressing mutated BRCA1^{5382insC} had inherent 8-OxoG accumulation, unlike cells expressing wild-type BRCA1, there may be differences in the wild-type and mutated proteins that influence these processes.

To learn more about the biochemical differences between wild-type BRCA1 and mutated BRCA1^{5382insC} under oxidative conditions, we accessed protein levels in nuclear extracts. Western blot analysis performed on replicate experiments showed that BRCA1^{5382insC} and BARD1 levels were reduced in H_2O_2-treated cells. Wild-type proteins from two different cell sources (HCC70 and HCC70-R lines) were rather immune to the H_2O_2 treatment. Polyclonal antibodies against the BRCT domain of BRCA1 were used for detection to ensure an adequate comparison of protein signals, considering that the RING domain may be less accessible, according to results in Fig. 3C. BRCA1^{5382insC} migrated at ~270 kDa, slower than the phosphorylated form of wild-type BRCA1 (Fig. 3F). As an independent control, we evaluated RAD51 levels, which were stable in the nucleus during treatment. Together, the data indicate that oxidative stress alters the structure and the function of BRCA1^{5382insC} in breast cancer cells. These observations were consistent with other studies on mutated BRCA1, which show that its DNA repair function is reduced during stressful situations (*10*–*14*). We then questioned, can we better manage inadequacies in mutated BRCA1?

Modified BRCA1^{5382insC}-BARD1 is altered by deubiquitinase treatment

The biophysical evidence presented here shows that cellular stress changes the molecular properties of mutated BRCA1. The evidence includes (i) a shift in the mobility of BRCA1^{5382insC} in SDS-PAGE and Western blot analysis, (ii) limited accessibility of the BRCA1^{5382insC} RING domain, and (iii) extra density in the BRCA1^{5382insC}-BARD1 structure proximal to the RING domain. To further test whether ubiquitination accounts for these changes, we evaluated protein fractions from cells undergoing oxidative stress and treated with the deubiquitinase (DUB) enzyme, ubiquitin-specific protease 2 (USP2). USP2 removes a variety of ubiquitin adducts from protein substrates, generating monoubiquitin (~8 kDa) upon removal. Protein fractions of BRCA1^{5382insC}-BARD1 isolated from H_2O_2-treated cells were incubated with catalytically active USP2 (500 nM; Boston Biochem) in Hepes buffer (pH 7.5) for 30 min at 37°C. Control fractions received a Hepes buffer solution lacking USP2.

The biochemical analysis of USP2-treated fractions across replicate experiments showed a shift in BRCA1^{5382insC} mobility from ~270 kDa back to ~260 kDa. This band shift was consistent across multiple Western blots probed with antibodies against the BRCT and RING domains of BRCA1 (Fig. 4A). Treated and control samples contained equal quantities of BRCA1^{5382insC}, as indicated by equal detection of the BRCT domain. USP2-treated samples further showed a marked increase in the detection of the BRCA1^{5382insC} RING domain. Ubiquitinated products were also present in the control sample at ~270 kDa, and these bands were generally reduced in the USP2-treated fractions. Moreover, we detected a significant increase in monoubiquitin at the expected molecular weight of ~8 kDa in the treated fractions compared to the control samples (Fig. 4A).

To understand these biochemical changes in the context of the 3D structure, we used single-particle EM to examine deubiquitinated BRCA1^{5382insC}-BARD1. Images and class averages of USP2-treated BRCA1^{5382insC}-BARD1 (Fig. 4B) closely resembled the unmodified form of the heterodimer. The particles were less compact in nature and maintained the conserved clamp-shaped architecture. Again, particle orientations were not limited in the USP2-treated structure, and the density map was refined to 15.4 Å using RELION and verified by RMEASURE (fig. S4).

The 3D structure of deubiquitinated BRCA1^{5382insC}-BARD1 lacked the extra density in the hotspot region adjacent to the RING domain (Fig. 4C and movie S4). To better visualize this change, we calculated a difference map between comparable regions of the H_2O_2-treated BRCA1^{5382insC}-BARD1 structure and the USP2-treated BRCA1^{5382insC}-BARD1 structure (Fig. 4D). We implemented the same density threshold procedures described for Fig. 3 to highlight changes in the BRCA1 hotspot area. The resulting difference peak (Fig. 4D, yellow) shows the additional density that is present in the BRCA1^{5382insC}-BARD1 structure upon H_2O_2 treatment but is lacking in the same region of the USP2-treated BRCA1^{5382insC}-BARD1 structure.

The lack of density in the deubiquitinated BRCA1^{5382insC}-BARD1 structure is a clear indicator that ubiquitin moieties were distinctly removed from the BRCA1 hotspot area. There were also minor differences found in the molecular structure at the BRCT domain. However, these differences are likely due to enhanced flexibility or conformational variability in the mutated BRCT domain during oxidative stress and showed no signs of ubiquitin density. Overall, both the 2D averages and the 3D structure of USP2-treated BRCA1^{5382insC}-BARD1 demonstrate that a modified, less functional form of BRCA1 can be modulated to restore its structural integrity.

DISCUSSION

In summary, we present the first structural information for full-length BRCA1-BARD1 isolated from human breast cancer cells. Structures formed under a variety of cellular conditions allowed us to directly compare wild-type and mutated complexes. Each of the 3D structures adopted a conserved clamp-like motif with characteristic features found in other E3 ubiquitin ligases (*29*–*31*). Under normal growth conditions, there were subtle differences between wild-type and mutated structures. For example, the BRCT domain of mutated BRCA1 was slightly truncated, resulting in less density in this region of the reconstruction. In general, E3 ubiquitin ligases bring E2-conjugating enzymes in proximity to a substrate. The substrate-binding region of BRCA1 resides in the BRCT domain. Hence, mutations that affect the structural properties of the BRCT can influence BRCA1's ability to transfer ubiquitin moieties to its substrates.

Under oxidative conditions, the mutated BRCA1-BARD1 structure showed attributes that were not present in the wild-type or untreated structures. To better understand these changes, we performed additional biochemical experiments. These studies revealed that BRCA1^{5382insC} migrated more slowly than wild-type BRCA1 on Western blot analysis, and the RING domain was less exposed in the mutated protein. Work by others determined that residues surrounding the BRCA1 RING domain can be ubiquitinated, phosphorylated, or sumoylated (*32*–*34*). Ubiquitin adducts were present in this region on mutated BRCA1 under oxidative conditions. This observation agrees with the work of Lu *et al.* (*17*) who first discovered the degron sequence of BRCA1 in ovarian cancer patients.

The general mechanisms by which ubiquitination is involved in the DNA damage response is dynamic and complex. BRCA1 is one of many players that orchestrate protective measures against genotoxic

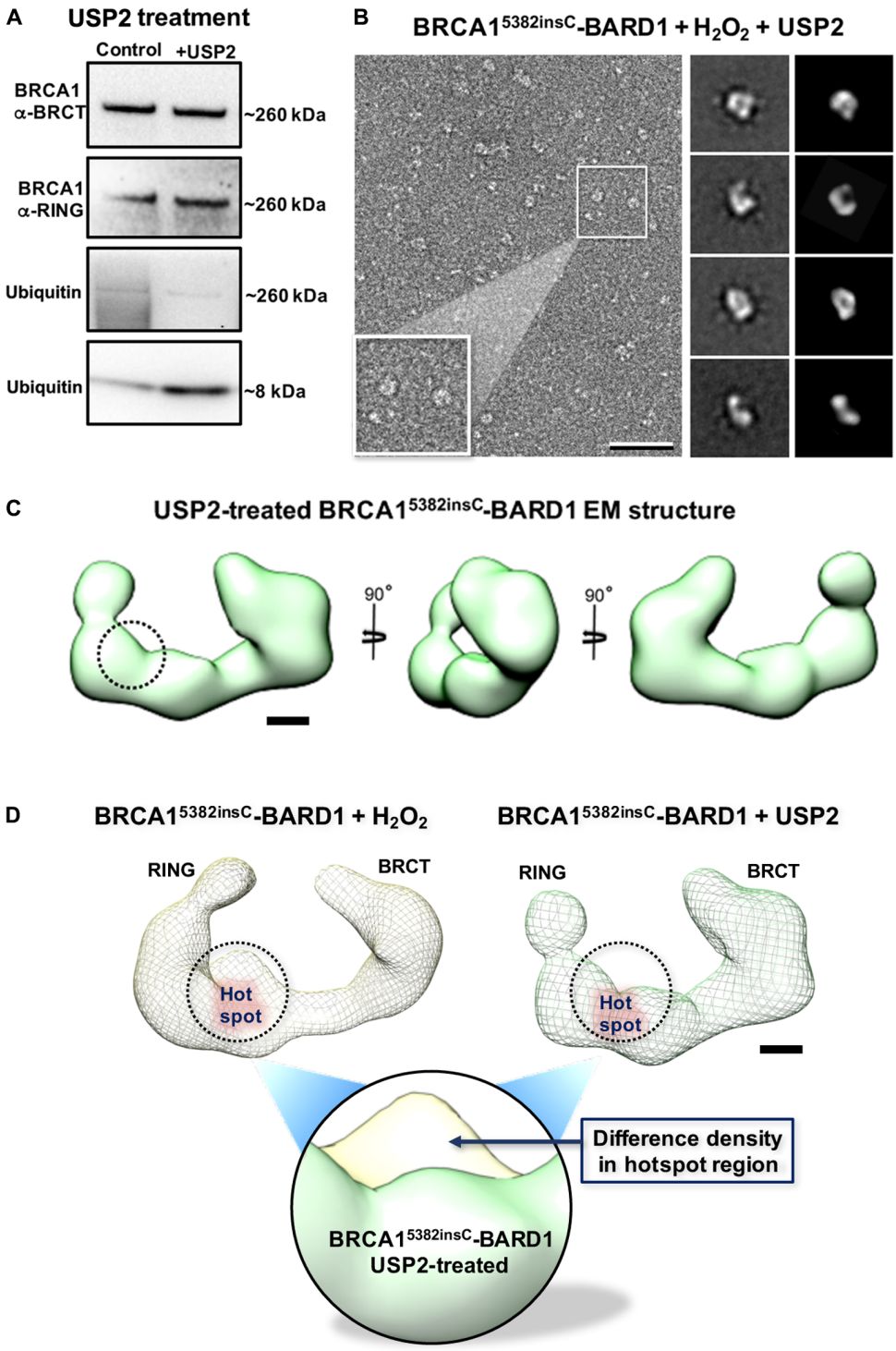

Fig. 4. DUB treatment of BRCA1^{5382insC}-BARD1 restores structural integrity. (**A**) Western blot analysis of USP2-treated protein fractions isolated from HCC1937 cells experiencing oxidative stress. The band shift for BRCA1^{5382insC} to ~260 kDa in USP2-treated samples was confirmed by probing the BRCT and RING domains of BRCA1. Greater signal for the RING domain was detected in the USP2-treated samples along with a reduced signal for ubiquitin attachments at ~260 kDa. Increased levels of monoubiquitin (~8 kDa) were found in USP2-treated samples. (**B**) Image (left) and class averages (center) of mutated BRCA1^{5382insC}-BARD1 treated with 1 mM H_2O_2 and USP2. Scale bar, 50 nm. Projections of the 3D structure (right) agree with the class averages. Box size of averages, 25 nm. (**C**) The EM structure of BRCA1^{5382insC}-BARD1 shows a clamp-like motif lacking extra density adjacent to the RING domain (black circle) (fig. S4 and movie S4). Scale bar, 1.5 nm. (**D**) Difference peak (yellow) indicates the additional mass present in the hotspot region of BRCA1^{5382insC} under oxidative conditions. This area of extra mass is lacking in the USP2-treated BRCA1^{5382insC}-BARD1 structure (green).

insults. Other examples of ubiquitination playing a role in DNA repair involve regulatory events surrounding histone H2A modifications. USP51 was recently shown to deubiquitinate H2A at Lys^{13} and Lys^{15} during double-stranded breaks resulting from ionizing radiation. This loss of ubiquitin signal on H2A prevented the proper recruitment of repair proteins to DNA lesions (*35*). Another recent study on H2A ubiquitination during ultraviolet-induced nuclear excision repair processes pinpoints the biochemical players and steps involved in chromatin remodeling through the zuotin-related factor 1 (ZRF1) molecular switch (*36*). A complementary role for BRCA1 in ubiquitinating H2A at sites of DNA damage has also been well established (*37*). However, BRCA1's ability to perform this important task is reduced as protein levels are diminished, or its functional N- and C-terminal domains are compromised.

Our recent biochemical studies demonstrated that increases in K48 ubiquitination can lower functional levels of mutated BRCA1 in cellular assays (*16*). The structural analysis presented here further explains how mutated BRCA1 is affected by detrimental ubiquitination events. Because irregularities in the BRCA1 structure were linked to functional deficiencies in cancer cells, it is intriguing to think that the restoration of BRCA1's structural properties may improve its cellular activity. Ongoing efforts to test this idea are promising but fall outside the scope of the current report.

Overall, our results provide a unique outlook on the structure-function relationship of BRCA1 that is currently missing in the field. We found that deficiencies in mutated BRCA1 were related to unwarranted ubiquitination in cells experiencing oxidative stress. Cells deficient in BRCA1 activity tend to accumulate DNA insults that provide a tipping point toward cancer induction (*2*, *14*). In contrast, we show that detrimental changes to mutated BRCA1 can be biochemically tempered to renew its structural integrity. Further investigation of this paradigm on a functional level can provide new mechanistic insights into therapeutic intervention.

MATERIALS AND METHODS

Authentication of cells, cell culture, and protein enrichment

Breast cancer cells (HCC70 and HCC1937 lines) used in this study were purchased from ATCC and independently characterized by ATCC as triple-negative primary ductal carcinoma cells. For all experiments, cells were promptly used within 6 months of resuscitation. Cells were cultured in RPMI 1640 (Mediatech) supplemented with 10% fetal bovine serum (ATCC) and 0.5× penicillin-streptomycin (Thermo Fisher Scientific) at 37°C and 5% CO_2. BRCA1-BARD1 complexes were enriched as previously described (*25*). Briefly, ~1 million cells were collected using trypsin-EDTA (Thermo Fisher Scientific) followed by centrifugation (500*g*; 5 min). For experiments involving H_2O_2, cells were collected with cell scrapers after treatment with 1 mM H_2O_2 (Sigma-Aldrich) for 40 min at 37°C and 5% CO_2. Subcellular fractions (cytoplasmic and nuclear) were separated using the NE-PER kit (Thermo Fisher Scientific). The soluble nuclear material was incubated with Ni-NTA agarose beads (Qiagen) and incubated with rotation for 1 hour at 4°C. The beads were washed with five bed volumes of 20 mM Hepes buffer (pH 7.2; 140 mM NaCl, 2 mM $CaCl_2$, 2 mM $MgCl_2$, and 5 mM imidazole). Phosphorylated BRCA1-BARD1 naturally bound to the Ni-NTA column matrix and was eluted in the same Hepes buffer, supplemented with 150 mM imidazole. Protein concentrations were determined using the standard Pierce Bradford assay (Thermo Fisher Scientific).

Coomassie blue staining and immunoblot analysis

Protein fractions were analyzed by SDS-PAGE followed by either Coomassie blue staining or Western blotting. Proteins were separated on 3 to 8% tris-acetate NuPAGE mini gels (Thermo Fisher Scientific) and stained by SimplyBlue SafeStain solutions (Invitrogen) for 60 min. Gels were washed with deionized water for 60 min and then 3% NaCl for an additional 2 hours—overnight to achieve maximum sensitivity. Western blots were performed as described previously (*16*). The following primary antibodies were used in our analysis: BRCA1-C20 (SCBT, sc-642; α-BRCT), BRCA1-Ab1 (Calbiochem, OP92; α-RING), BRCA1-A8X9F (Cell Signaling Technology, #14823; α-RING), BARD1 (SCBT, sc-11438), ubiquitin-pAb (Enzo Life Sciences, ADI-SPA-200), RAD51 (SCBT, sc-8349), and β-actin (Sigma-Aldrich, A5441).

Co-IP analysis

To detect protein-protein interactions, co-IP experiments were performed on isolated BRCA1-BARD1 protein fractions using previously described procedures (*16*). Antibodies used for IP experiments included BRCA1-C20 (5 μg; SCBT, sc-642) and BARD1 (5 μg; SCBT, sc-11438).

DUB assay

$BRCA1^{5382insC}$-BARD1 protein fractions isolated from H_2O_2-treated cells were used for DUB assays. The reaction mixture (total volume, 200 μl) contained 180 μl of the protein fraction and 20 μl of 10× USP2 catalytic domain (final concentration, 500 nM; UbiCREST, K-400; Boston Biochem). Control mixtures were prepared with 180 μl of the protein fraction and 20 μl of 1× DUB reaction buffer (UbiCREST, K-400; Boston Biochem) lacking the enzyme. Both reaction and control tubes were incubated in a water bath at 37°C. After 30 min, samples were directly analyzed by either EM imaging or SDS-PAGE and Western blot analysis. Before EM specimen preparation, free ubiquitin was removed from the samples using Pierce Concentrator (100K MWCO, 0.5 ml; Thermo Fisher Scientific).

EM specimen preparation and imaging

Samples of isolated wild-type, mutated, and modified BRCA1-BARD1 assemblies [0.02 mg/ml in 20 mM Hepes buffer (pH 7.2), 150 mM NaCl, 10 mM $CaCl_2$, 10 mM $MgCl_2$] were applied to glow-discharged, continuous carbon support films on copper grids (Ted Pella) or to EM affinity grids (*24*, *38*). Affinity grids were decorated with antibodies against the BRCA1 RING domain (EMD Millipore; MS110, AB1) or the BRCT domain (C-20) for labeling studies conducted on wild-type assemblies. Protein complexes were tethered to the antibody-decorated grids by incubating Ni-NTA eluates for 2 min, followed by standard negative staining procedures using 1% uranyl formate (*39*). Specimens were examined using a FEI TEM (FEI Company) equipped with a LaB6 filament and operating at 120 kV under low-dose conditions (<5 electrons/$Å^2$). Images were recorded using an Eagle 2k HS CCD camera (FEI Company) with a pixel size of 30 μm at a magnification of about ×68,000 for a final sampling of 4.4 Å/pixel.

Image processing

Image processing procedures are summarized schematically in table S1. Individual particles were selected from the EM images using the SPIDER software package (*21*). Selected particles were subjected to reference-free alignment routines implementing *k*-means classification to compute 2D class averages. Particles contained in the averages were grouped into image stacks and exported to the RELION software

package (*22*). The RELION software package was used to refine and reconstruct the individual complexes using an initial model of a sphere having a diameter of ~120 Å. The model was used in the initial round of refinement. Later iterations were heavily dependent on the experimental data to refine the assigned angles by setting the regularization parameter to $T = 4$. We followed standard reconstruction routines and used a pixel size of 4.4 Å to produce 3D structures masked at ~120 Å. Equivalent contour levels were used to compare the EM maps among the various structures in the Chimera program (*40*). Threshold values for display are indicated in the EM map depositions and accommodated molecular volumes equivalent to ~320 to 350 kDa and 120 Å in diameter.

Particle heterogeneity for each sample was evaluated at the 2D and 3D classification steps. Class averages were calculated separately for each sample that included (i) wild-type BRCA1-BARD1, (ii) mutated BRCA1-BARD1, (iii) mutated BRCA1-BARD1 (H_2O_2-treated), and (iv) mutated BRCA1-BARD1 (USP2-treated). Particles in the 2D averages that displayed high-contrast features and were sufficiently separated from other particles were used for reconstruction routines in RELION. This inspection procedure is a standard practice in the EM field (*22*). At the level of 3D classification, RELION parameters were first implemented to output three to five classes from each image stack. For each sample, statistical values output from RELION following 25 iterations of refinement indicated that the particle data could be combined into a single composite structure. Composite structures were subsequently calculated for each sample using the same input parameters. The final density maps are shown in Figs. 1 to 4. The resolution of each map was determined by dividing the particle data for each reconstruction into two halves and calculating separate density maps. We used the 0.5 FSC criteria to determine the final resolution of each structure and then independently verify these values using the RMEASURE program (*26*). The final structure of the wild-type BRCA1-BARD1 (14.5 Å) contained 4008 particles. The structure of the mutated untreated $BRCA1^{5382insC}$-BARD1 (14.7 Å) contained 4222 particles, whereas the structure of the mutated H_2O_2-treated $BRCA1^{5382insC}$-BARD1 (15.6 Å) contained 4103 particles. The USP2-treated $BRCA1^{5382insC}$-BARD1 structure (15.4 Å) contained 4000 particles.

Difference maps

We calculated difference densities between the H_2O_2-treated $BRCA1^{5382insC}$-BARD1 map and the untreated $BRCA1^{5382insC}$-BARD1 map. Maps were normalized and, to a common density range and differences, were generated using the publicly available DIFFMAP.exe. Difference densities in comparable regions at or above a 3σ threshold were considered significant (*28*). A second difference map was calculated using the same procedures to visualize significant differences between the H_2O_2-treated $BRCA1^{5382insC}$-BARD1 map and the USP2-treated $BRCA1^{5382insC}$-BARD1 map.

Movie production

The Chimera software package (*40*) was used to produce each movie. Each structure was similarly orientated, and a python file of the scene was exported. After this routine, a Chimera command file was produced for each structure. These files contain a list of command line instructions that Chimera parses and applies to the scene. At the beginning of each movie, a trio of labels are generated to indicate the location of the RING and BRCT domains and the hotspot region. For cross-sectional views, camera slices were produced over a period of 110 frames. This procedure was reversed, as frame slices were replaced. Each structure was rotated about the *x* axis by 1° per frame for 90 frames. The slicing procedure was repeated and then reversed again. For rotated views, each structure was rotated about the *y* axis by 2° per frame for 45 frames (90°). The labels to indicate the hotspot region along with the RING and BRCT domains appear accordingly.

SUPPLEMENTARY MATERIALS

Supplementary material for this article is available at http://advances.sciencemag.org/cgi/content/full/3/9/e1701386/DC1

fig. S1. Biochemical characterization of wild-type BRCA1-BARD1.
fig. S2. Biochemical characterization of mutated $BRCA1^{5382insC}$-BARD1.
fig. S3. Changes in the properties of the $BRCA1^{5382insC}$-BARD1 under oxidative conditions.
fig. S4. The $BRCA1^{5382insC}$-BARD1 structure is restored following USP2 treatment.
movie S1. Movie of the wild-type BRCA1-BARD1 structure.
movie S2. Movie of the mutated $BRCA1^{5382insC}$-BARD1 structure.
movie S3. Movie of mutated $BRCA1^{5382insC}$-BARD1 isolated from H_2O_2-treated cells.
movie S4. Movie of mutated $BRCA1^{5382insC}$-BARD1 treated with USP2.
table S1. Flow chart of image processing procedures including steps for assessing particle heterogeneity during 2D averaging and 3D classification procedures.

REFERENCES AND NOTES

1. P. L. Welcsh, K. N. Owens, M.-C. King, Insights into the functions of BRCA1 and BRCA2. *Trends Genet.* **16**, 69–74 (2000).
2. S. Rowell, B. Newman, J. Boyd, M. C. King, Inherited predisposition to breast and ovarian cancer. *Am. J. Hum. Genet.* **55**, 861–865 (1994).
3. E. M. Rosen, S. Fan, Y. Ma, BRCA1 regulation of transcription. *Cancer Lett.* **236**, 175–185 (2006).
4. D. J. Toft, V. L. Cryns, Minireview: Basal-like breast cancer: From molecular profiles to targeted therapies. *Mol. Endocrinol.* **25**, 199–211 (2011).
5. C. M. Perou, Molecular stratification of triple-negative breast cancers. *Oncologist* **15** (suppl. 5), 39–48 (2010).
6. P. Schwertman, S. Bekker-Jensen, N. Mailand, Regulation of DNA double-strand break repair by ubiquitin and ubiquitin-like modifiers. *Nat. Rev. Mol. Cell Biol.* **17**, 379–394 (2016).
7. W. Wu, A. Koike, T. Takeshita, T. Ohta, The ubiquitin E3 ligase activity of BRCA1 and its biological functions. *Cell Div.* **3**, 1–10 (2008).
8. R. Baer, T. Ludwig, The BRCA1/BARD1 heterodimer, a tumor suppressor complex with ubiquitin E3 ligase activity. *Curr. Opin. Genet. Dev.* **12**, 86–91 (2002).
9. P. S. Brzovic, J. R. Keeffe, H. Nishikawa, K. Miyamoto, D. Fox III, M. Fukuda, T. Ohta, R. Klevit, Binding and recognition in the assembly of an active BRCA1/BARD1 ubiquitin-ligase complex. *Proc. Natl. Acad. Sci. U.S.A.* **100**, 5646–5651 (2003).
10. I. Bae, S. Fan, Q. Meng, J. K. Rih, H. J. Kim, H. J. Kang, J. Xu, I. D. Goldberg, A. K. Jaiswal, E. M. Rosen, BRCA1 induces antioxidant gene expression and resistance to oxidative stress. *Cancer Res.* **64**, 7893–7909 (2004).
11. F. Le Page, V. Randrianarison, D. Marot, J. Cabannes, M. Perricaudet, J. Feunteun, A. Sarasin, BRCA1 and BRCA2 are necessary for the transcription-coupled repair of the oxidative 8-oxoguanine lesion in human cells. *Cancer Res.* **60**, 5548–5552 (2000).
12. E. Alli, V. B. Sharma, P. Sunderesakumar, J. M. Ford, Defective repair of oxidative DNA damage in triple-negative breast cancer confers sensitivity to inhibition of poly(ADP-ribose) polymerase. *Cancer Res.* **69**, 3589–3596 (2009).
13. E. Alli, J. M. Ford, BRCA1: Beyond double-strand break repair. *DNA Repair* **32**, 165–171 (2015).
14. U. E. Martinez-Outschoorn, R. Balliet, Z. Lin, D. Whitaker-Menezes, R. C. Birbe, A. Bombonati, S. Pavlides, R. Lamb, S. Sneddon, A. Howell, F. Sotgia, M. P. Lisanti, BRCA1 mutations drive oxidative stress and glycolysis in the tumor microenvironment: Implications for breast cancer prevention with antioxidant therapies. *Cell Cycle* **11**, 4402–4413 (2012).
15. D. Hanahan, R. A. Weinberg, Hallmarks of cancer: The next generation. *Cell* **144**, 646–674 (2011).
16. B. L. Gilmore, Y. Liang, C. E. Winton, K. Patel, V. Karageorge, A. C. Varano, W. Dearnaley, Z. Sheng, D. F. Kelly, Molecular analysis of BRCA1 in human breast cancer cells under oxidative stress. *Sci. Rep.* **7**, 43435 (2017).
17. Y. Lu, A. Amleh, J. Sun, X. Jin, S. D. McCullough, R. Baer, D. Ren, R. Li, Y. Hu, Ubiquitination and proteasome-mediated degradation of BRCA1 and BARD1 during steroidogenesis in human ovarian granulosa cells. *Mol. Endocrinol.* **21**, 651–663 (2007).
18. P. S. Brzovic, P. Rajagopal, D. W. Hoyt, M. C. King, R. E. Klevit, Structure of a BRCA1–BARD1 heterodimeric RING–RING complex. *Nat. Struct. Biol.* **8**, 833–837 (2001).

19. R. S. Williams, R. Green, J. N. M. Glover, Crystal structure of the BRCT repeat region from the breast cancer-associated protein BRCA1. *Nat. Struct. Biol.* **8**, 838–842 (2001).
20. A. F. Gazdar, V. Kurvari, A. Virmani, L. Gollahon, M. Sakaguchi, M. Westerfield, D. Kodagoda, V. Stasny, H. T. Cunningham, I. I. Wistuba, G. Tomlinson, V. Tonk, R. Ashfaq, A. M. Leitch, J. D. Minna, J. W. Shay, Characterization of paired tumor and non-tumor cell lines established from patients with breast cancer. *Int. J. Cancer* **78**, 766–774 (1998).
21. J. Frank, M. Radermacher, P. Penczek, J. Zhu, Y. Li, M. Ladjadj, A. Leith, SPIDER and WEB: Processing and visualization of images in 3D electron microscopy and related fields. *J. Struct. Biol.* **116**, 190–199 (1996).
22. S. H. W. Scheres, A Bayesian view on cryo-EM structure determination. *J. Mol. Biol.* **415**, 406–418 (2012).
23. D. Lyumkis, S. K. Doamekpor, M. H. Bengtson, J.-W. Lee, T. B. Toro, M. D. Petroski, C. D. Lima, C. S. Potter, B. Carragher, C. A. P. Joazeiro, Single-particle EM reveals extensive conformational variability of the Ltn1 E3 ligase. *Proc. Natl. Acad. Sci. U.S.A.* **110**, 1702–1707 (2013).
24. D. F. Kelly, D. Dukovski, T. Walz, Strategy for the use of affinity grids to prepare non-His-tagged macromolecular complexes for single-particle electron microscopy. *J. Mol. Biol.* **400**, 675–681 (2010).
25. B. L. Gilmore, C. E. Winton, A. C. Demmert, J. R. Tanner, S. Bowman, V. Karageorge, K. Patel, Z. Sheng, D. F. Kelly, A molecular toolkit to visualize native protein assemblies in the context of human disease. *Sci. Rep.* **5**, 14440 (2015).
26. D. Sousa, N. Grigorieff, Ab initio resolution measurement for single particle structures. *J. Struct. Biol.* **157**, 201–210 (2007).
27. G. E. Tomlinson, T. T.-L. Chen, V. A. Stastny, A. K. Virmani, M. A. Spillman, V. Tonk, J. L. Blum, N. R. Schneider, I. I. Wistuba, J. W. Shay, J. D. Minna, A. F. Gazdar, Characterization of a breast cancer cell line derived from a germ-line BRCA1 mutation carrier. *Cancer Res.* **58**, 3237–3242 (1998).
28. J. Frank, *Three-Dimensional Electron Microscopy of Macromolecular Assemblies* (Oxford Univ. Press Inc., 2006).
29. G. Nalepa, M. Rolfe, J. W. Harper, Drug discovery in the ubiquitin–proteasome system. *Nat. Rev. Drug Discov.* **5**, 596–613 (2006).
30. C. E. Berndsen, C. Wolberger, New insights into ubiquitin E3 ligase mechanism. *Nat. Struct. Mol. Biol.* **21**, 301–307 (2014).
31. A. M. Simons, A. A. Horwitz, L. M. Starita, K. Griffin, R. S. Williams, J. N. Glover, J. D. Parvin, BRCA1 DNA-binding activity is stimulated by BARD1. *Cancer Res.* **66**, 2012–2018 (2006).
32. A. D. Choudhury, H. Xu, R. Baer, Ubiquitination and proteasomal degradation of the BRCA1 tumor suppressor is regulated during cell cycle progression. *J. Biol. Chem.* **279**, 33909–33918 (2004).
33. C.-X. Deng, BRCA1: Cell cycle checkpoint, genetic instability, DNA damage response and cancer evolution. *Nucleic Acids Res.* **34**, 1416–1426 (2006).
34. J. R. Morris, C. Boutell, M. Keppler, R. Densham, D. Weekes, A. Alamshah, L. Butler, Y. Galanty, L. Pangon, T. Kiuchi, T. Ng, E. Solomon, The SUMO modification pathway is involved in the BRCA1 response to genotoxic stress. *Nature* **462**, 886–890 (2009).
35. Z. Wang, H. Zhang, J. Liu, A. Cheruiyot, J.-H. Lee, T. Ordog, Z. Lou, Z. You, Z. Zhang, USP51 deubiquitylates H2AK13,15ub and regulates DNA damage response. *Genes Dev.* **30**, 946–959 (2016).
36. E. Gracheva, S. Chitale, T. Wilhelm, A. Rapp, J. Byrne, J. Stadler, R. Medina, M. C. Cardoso, H. Richly, ZRF1 mediates remodeling of E3 ligases at DNA lesion sites during nucleotide excision repair. *J. Cell Biol.* **213**, 185–200 (2016).
37. R. Kalb, D. L. Mallery, C. Larkin, J. T. J. Huang, K. Hiom, BRCA1 is a histone-H2A-specific ubiquitin ligase. *Cell Rep.* **8**, 999–1005 (2014).
38. C. E. Winton, B. L. Gilmore, A. C. Demmert, V. Karageorge, Z. Sheng, D. F. Kelly, A microchip platform for structural oncology applications. *NPJ Breast Cancer* **2**, 16016 (2016).
39. M. Ohi, Y. Li, Y. Cheng, T. Walz, Negative staining and image classification—Powerful tools in modern electron microscopy. *Biol. Proced. Online* **6**, 23–34 (2004).
40. E. F. Pettersen, T. D. Goddard, C. C. Huang, G. S. Couch, D. M. Greenblatt, E. C. Meng, T. E. Ferrin, UCSF Chimera—A visualization system for exploratory research and analysis. *J. Comput. Chem.* **25**, 1605–1612 (2004).

Acknowledgments

Funding: This work was supported by funds from the Commonwealth Health Research Board (2080914), the Concern Foundation (303872), NIH/National Cancer Institute (1R01CA193578-01A1), and the University of Virginia–Virginia Tech Carilion Neuroscience Seed Fund Award. **Author contributions:** Y.L., A.C.V., C.E.W., and B.L.G. assisted in cell culture experiments, prepared BRCA1 assemblies, and performed biochemical assessments including co-IP experiments. Y.L. performed fluorescence microscopy and Western blot analysis. Z.S. provided microscopy support and reagents. C.E.W., Y.L., and W.J.D. prepared EM specimens. C.E.W., W.J.D., N.A.A., and D.F.K. collected EM images and performed image processing calculations. Y.L., W.J.D., A.C.V., Z.S., and D.F.K. helped with experimental design and wrote the manuscript. **Competing interests:** The authors declare that they have no competing interests. **Data and materials availability:** All data needed to evaluate the conclusions in the paper are present in the paper and/or the Supplementary Materials. Additional data related to this paper may be requested from the authors. EM structures for wild-type BRCA1-BARD1 (EMD-8833) and mutated BRCA1-BARD1 (EMD-8834) are being deposited in the EMDataBank and can be freely downloaded at www.emdatabank.org.

Submitted 9 May 2017
Accepted 30 August 2017
Published 20 September 2017
10.1126/sciadv.1701386

Citation: Y. Liang, W. J. Dearnaley, A. C. Varano, C. E. Winton, B. L. Gilmore, N. A. Alden, Z. Sheng, D. F. Kelly, Structural analysis of BRCA1 reveals modification hotspot. *Sci. Adv.* **3**, e1701386 (2017).